Competitive Effects of Surface Plasmon Resonances and Interband Transitions on Plasmon-Enhanced Second-Harmonic Generation at Near-Ultraviolet Frequencies

Shaoxin Shen,[1,2,*] Jiejie Shan,[3] Tien-Mo Shih,[4] Junbo Han,[5] Zongwei Ma,[5] Feng Zhao,[1] Fangzu Yang,[3] Yongliang Zhou,[3] and Zhilin Yang[1,†]

[1] *Department of Physics, Collaborative Innovation Center for Optoelectronic Semiconductors and Efficient Devices, Xiamen University, Xiamen 361005, People's Republic of China*

[2] *College of Information Science and Engineering, Fujian Provincial Key laboratory of Light Propagation and Transformation, Huaqiao University, Xiamen 361021, People's Republic of China*

[3] *State Key Laboratory of Physical Chemistry of Solid Surfaces, Xiamen University, Xiamen 361005, People's Republic of China*

[4] *Department of Mechanical Engineering, University of California at Berkeley, Berkeley, California 94720, USA*

[5] *Wuhan National High Magnetic Field Center, Huazhong University of Science and Technology, Wuhan 430074, People's Republic of China*

(Received 9 September 2019; revised manuscript received 19 December 2019; accepted 3 February 2020; published 19 February 2020)

The competition between plasmonic resonances and noble-metal interband transitions at near-ultraviolet (NUV) frequencies complicates nonlinear conversion processes at nanoscales. Here, we experimentally design a highly enhanced and reproducible plasmon-enhanced second-harmonic generation (PESHG) platform suitable for NUV frequencies by constructing three-dimensional silver mushroom arrays. The SHG emission from proposed platforms involved in geometrical asymmetry greatly outperforms that from unpatterned metallic films. Studies among mushroom arrays with various geometric parameters and weight ratios of component materials enable us to distinguish characteristics exhibited by plasmon-driven enhancement and interband-transition suppression, such that competitive effects on PESHG can be readily observed and quantitatively measured. Our work may provide insights for understanding the physical mechanism governing plasmon-enhanced nonlinear optical processes and may help attain efficient nonlinear wavelength conversions for quantum-optical and nonlinear metamaterial applications.

DOI: 10.1103/PhysRevApplied.13.024045

I. INTRODUCTION

As a research focus of modern nonlinear nanophotonics, plasmon-enhanced second-harmonic generation (PESHG) has attracted much interest because of its promising applications to quantum information processing, nonlinear metasurfaces, and nanoscale light sources [1–5]. Due to high losses and inherently low nonlinear coefficients of traditional plasmonic materials, i.e., gold and silver, the requirement of boosting nonlinear frequency conversion at relatively low excitation powers becomes a significant precondition for understanding the mechanism that governs PESHG processes. For purposes of acquiring higher conversion efficiencies, studies have been dedicated to utilizing multiple-plasmon resonances over a broadband range, especially for doubly resonant designs both at fundamental and second-harmonic frequencies [6–8]. Notably, within multiresonant plasmonic nanostructures that respond to near-infrared or visible-light excitation, competition between noble-metal interband transitions and plasmon-driven resonances at near-ultraviolet (NUV) frequencies further complicates nonlinear conversion processes at nanoscales [9–11]. The primary reason is because of the occurrence of energy-loss channels, due to interband transitions of noble metals at NUV frequencies, which may lead to the potential damping of nonlinear polarization currents or selective reabsorption of PESHG signal emissions. Finding an efficient and reliable PESHG platform, which could quantitatively reveal competitive influences of interband transitions and plasmonic resonances on nonlinear optical scattering processes at NUV frequencies, constitutes a significant task. Furthermore, studies of PESHG in plasmonic structures have, so far, focused on planar or substrate-supported nanoparticle clusters with asymmetric geometries [6,7]. Less attention has been paid to engineering plasmonic materials in three dimensions by integrating the geometrical asymmetry in

*sxshen@hqu.edu.cn
†zlyang@xmu.edu.cn

periodic configurations. Particularly, the field enhancement of three-dimensional (3D) plasmonic nanodevices is not exclusively confined to the interface or the substrate, but mainly redistributed in air, offering additional degrees of freedom to modulate nonlinear wavelength conversions in a highly sensitive way [12–15].

Here, we propose and construct a model of 3D mushroom arrays to experimentally evaluate the quantitative influence of geometrical asymmetry and the tentatively coined effect of "interband-transition suppression to multimode matching" on the efficient generation of NUV light induced by nonlinear conversion processes. These proposed mushroom arrays are characterized by reduced 3D centrosymmetry relative to symmetrically oriented nanoparticles. They contribute to the remarkable enhancement of PESHG performances compared with the unpatterned metallic film at all frequencies participating in signal emissions, ranging from visible to NUV spectra. By means of constructing mushroom arrays with various weight ratios of component materials, we can reveal phenomena in which energy transfers from dominant interband-transition suppression to that of plasmon-driven resonance during PESHG processes. Via tuning different geometry parameters, we can further obtain multiple-plasmon-driven resonances at relevant excitation and emission steps to amplify PESHG emissions at NUV frequencies, when noble-metal interband transitions are notably suppressed.

II. DESIGN AND CHARACTERIZATION

These metallic mushroom arrays with various weight ratios of silver to gold (Ag:Au) and different geometry parameters are designed and fabricated by utilizing nanoimprint lithography combined with an electrochemical deposition process. See the Supplemental Material [16] for detailed fabrication schemes. Figures 1(a)–1(c) show schematic illustrations of arrays made of silver mushrooms (SMA), gold mushrooms (GMA), and silver-film-coated gold mushrooms (SGMA), respectively. Coordinates are chosen such that mushroom arrays lie on the x-y plane [Fig. 1(a), inset]. Measurements of SHG are performed by focusing a tunable Ti:sapphire laser as the fundamental wave [$E(\omega)$, $\mathbf{k}_{in}$] onto samples from the air side (z direction) at an incident angle ($\theta = 45°$), while reflection-scattered SHG signals [$E(2\omega)$, $\mathbf{k}_{out}$] are collected by a CCD camera [Fig. 1(a)]. See the Supplemental Material [16] for detailed SHG experimental methods. Utilization of the oblique incident beam can reduce the 3D symmetry of mushroom arrays, inducing effective surface-enhanced nonlinear processes [13,17]. The size of the selected 40-μm-diameter incident-beam spot greatly surpasses that of mushrooms, assuring us of obtaining average signal performances. Figures 1(d) and 1(e) reveal that arrays of silver mushrooms grown on the flat gold substrate are made of stipes and pileuses, and the arrangement of mushroom units exhibits a high degree of homogeneity, leading to the achievement of uniform and reproducible responses. Gap sizes (g) between adjacent pileuses can be tuned at approximately 10 nm via optimizing the deposition time to optimize PESHG emissions. In the Supplemental Material [16], corresponding g-dependent mushroom arrays and SHG signal distributions are presented. In Fig. 1(f), energy-dispersive spectroscopy analyses display the change of the weight ratio of elements silver (Ag), gold (Au), carbon (C), and nitrogen (N), enabling us to characterize the evolution of SMA (Ag:Au, 99.46%), SGMA (Ag:Au, 10.23%), and GMA (Ag:Au, 0%).

III. NONLINEAR SCATTERING PROCESSES

As the first step of our experimental procedure, we introduce GMA to investigate the influence of the mushroomlike geometry on nonlinear wavelength conversions.

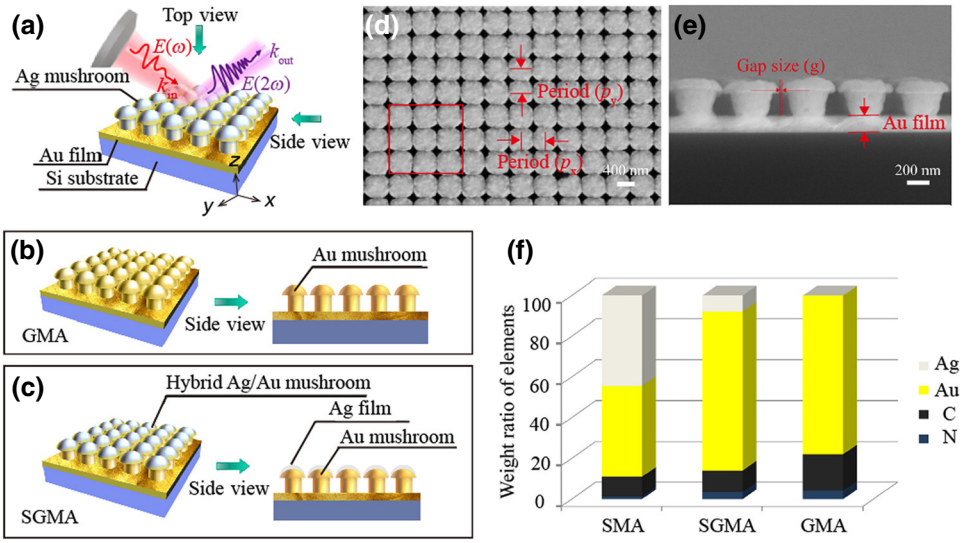

FIG. 1. Schematic illustration of (a) SMA, (b) GMA, and (c) SGMA. Inset in (a) exhibits schematic sketch of SHG measurements. (d) Top-view SEM image of SMA with 450-nm period along both x and y axes (p_x and p_y). The red-marked box shows the sampled region of energy-dispersive spectroscopy analyses. (e) Side-view SEM image of SMA with 220 nm stipe height and 300 nm diameter. (f) Energy-dispersive spectroscopy analyses of elements Ag, Au, C, and N for SMA, SGMA, and GMA. Elements C and N stem from residual photoresist layers.

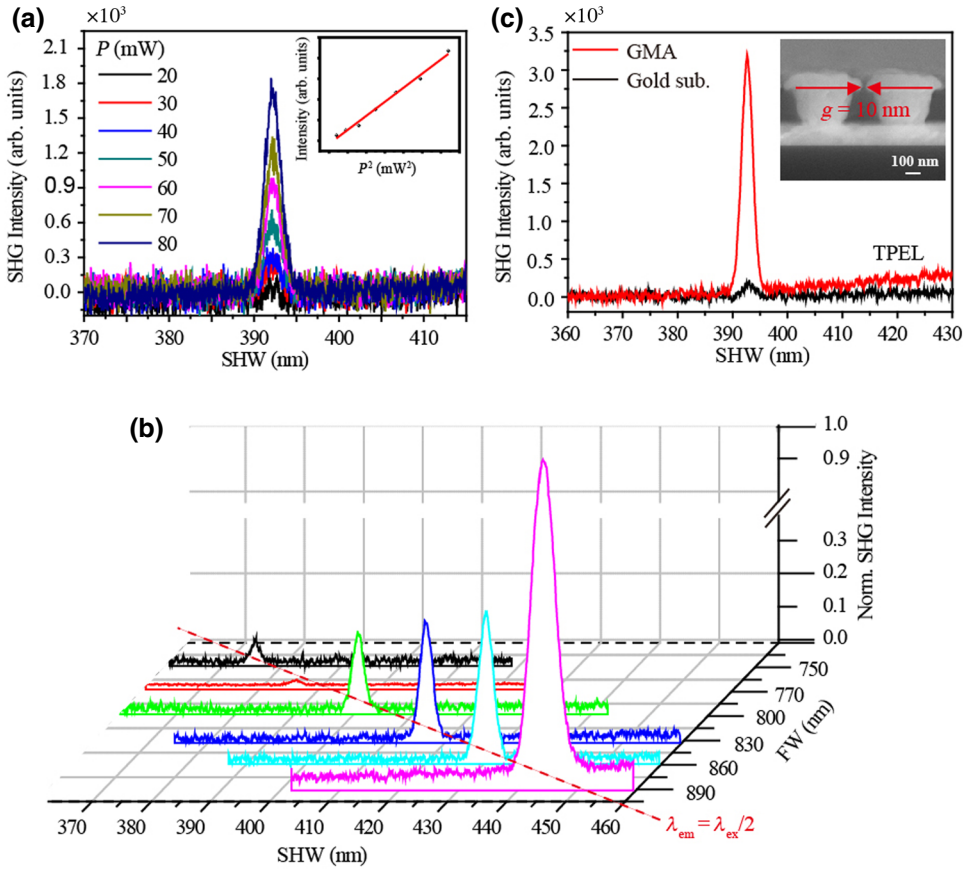

FIG. 2. (a) Power-dependent SHG measurements. Inset: measured SHG intensities versus the square of pumping powers, p^2. (b) Wavelength-dependent SHG measurements. All intensities are normalized by data at 445 nm. (c) A comparison of SHG performances between GMA (red line) and the bare gold substrate (gold sub., black line), where TPEL denotes two-photon-excited luminescence. Inset in (c) exhibits enlarged side-view SEM images of GMA.

As expected, measured signal intensities increase quadratically with the increasing excitation power, ranging from 20 to 80 mW. The SHG output remains stable under our pumping power range. Meanwhile, the emission peak position shifts from 375 to 445 nm by sweeping the excitation wavelength between 750 and 890 nm [Fig. 2(a) and 2(b)]. Experimental results agree satisfactorily with essential characteristics of SHG [18,19]. For the purpose of evaluating the nonlinearity activity, measurements are also taken on an unpatterned gold film with a 785 nm excitation wavelength and 60 mW power. As shown in Fig. 2(c), the SHG signal of GMA, which features a weak and broad two-photon-excited luminescence background [19], appears much stronger than that of unpatterned gold films. These results demonstrate the significant role of mushroomlike geometries played in the amplification of nonlinear scattering signals.

It is worth noting that signal intensities rapidly decrease as the emission frequency shifts from 445 to 375 nm [Fig. 2(b)]. The main reason stems from the occurrence of interband transitions in gold due to the threshold value of interband electron transitions equaling approximately 2.58 eV (480 nm wavelength) [11,20]. In a possible method that is capable of improving the external efficiency in measured spectral windows, plasmonic materials with higher interband-transition thresholds (such as silver or aluminum) can be introduced [11,21]. Especially, the interband-transition energy state of silver at approximately 3.93 eV [11,22], which is referenced to a wavelength of 315 nm, lies above measured spectral ranges [Fig. 3(a)]. We can reasonably deduce that interband transitions in gold can be avoided if silver components are adopted. Hence, we conduct a comparative study of PESHG performances between SMA and GMA by sweeping excitation wavelengths [Fig. 3(b)]. The result reveals that, through replacing gold mushrooms with silver ones, the emission power can be amplified at all frequencies, ranging from 445 to 375 nm, and the power distribution depends on the excitation frequency. It should be noted that, due to the oxidation of silver in SMA, a redshift of various reflection dips can be observed, resulting in the slow but inevitable decrease of SHG output powers. To quantitatively describe the discrepancy between GMA and SMA, we define the conversion efficiency as $\eta = P^a_{\mathrm{SH}}/P^a_{\mathrm{FF}}$, where P^a_{SH} and P^a_{FF} denote the second-harmonic (SH) and fundamental frequency (FF) average powers [23], with a constant slope of $\eta/P^a_{\mathrm{FF}} = P^a_{\mathrm{SH}}/(P^a_{\mathrm{FF}})^2$ (the power dependence of the SHG is quadratic with input laser power) [13,23]. In our experiments, the average power of the FF beam (P^a_{FF}) can be obtained in front of the sample via using a power meter. The average power of SH signals (P^a_{SH}) can be estimated by considering transmission

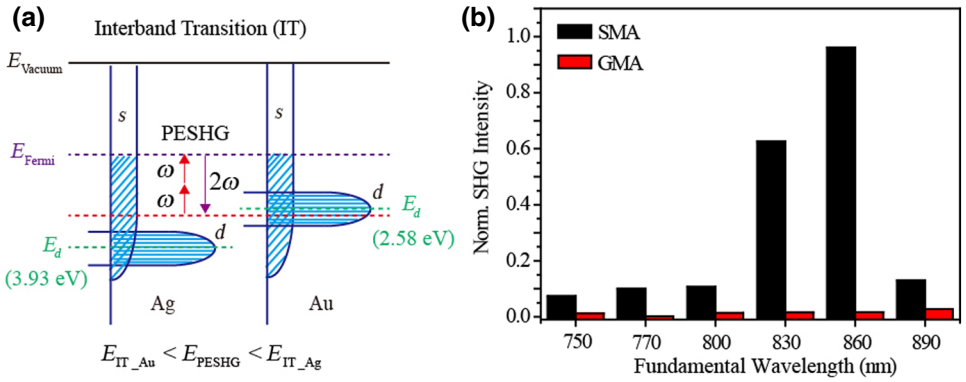

FIG. 3. (a) Schematic diagram of interband electron transitions in silver and gold. (b) Wavelength-dependent PESHG performances in SMA and GMA. All intensities are normalized by data for SMA at 860 nm.

coefficients of optical components and the quantum efficiency of the CCD detector. For a 60 mW average power of FF beams at both 860 and 890 nm, maximum conversion efficiencies of nominally 1.6×10^{-12} and 6.5×10^{-14}, respectively, are obtained for SMA and GMA. To illustrate a fairer comparison, we use the following figure of merit (FOM): $\xi = P^a_{SH}/(P^a_{FF})^2$ [23]. This FOM is thus independent of the pump power used for SHG. With this analysis, values of ξ for SMA and GMA are 2.7×10^{-11} and 1.1×10^{-12} W^{-1}, respectively. We can reasonably deduce that, in considering adopting component materials with higher interband-transition thresholds at NUV frequencies, the nonlinear signal enhancement reaches up to one order of magnitude.

To identify the underlying mechanism that governs this enhancement factor, we further experimentally perform a series of comparative studies to reveal the relative contribution of component-material dependences and frequency dependences in PESHG processes. In Fig. 4, measured reflectance spectra of GMA and SGMA both display plasmon-driven enhancements (red solid circles) near fundamental wavelengths ranging from 750 to 900 nm (red dashed lines). Near SH wavelengths (purple dashed lines), however, the contribution of plasmonic fields can be neglected in both samples, owing to the existence of off-resonance states in measured spectral windows (purple solid circles). Nevertheless, the measured SHG intensity distribution in GMA [Fig. 4(a), inset] shows a drastically decreasing trend as the emission wavelength shifts from 445 to 375 nm, even if a plasmonic field is excited at the fundamental wavelength of approximately 830 nm. This decreasing trend is most likely related to the onset of the interband-transition suppression, which occurs at this emission range for gold. More elaborately, it exhibits a dual-energy-loss channel, including the potential damping of nonlinear polarization currents and selective reabsorption of signal emissions, resulting in the severe suppression of plasmon-driven enhancements in PESHG processes. By contrast, through slightly reshaping weight ratios of component materials in mushrooms, such as depositing a thin silver film with 20-nm thickness onto the GMA surface (SGMA), the spectral position of SHG peak values agrees well with that of plasmon-driven enhancement at approximately 870 nm [Fig. 4(b), inset]. These analyses reveal that the mere addition of this silver film onto the GMA surface allows us to observe the dominance switching

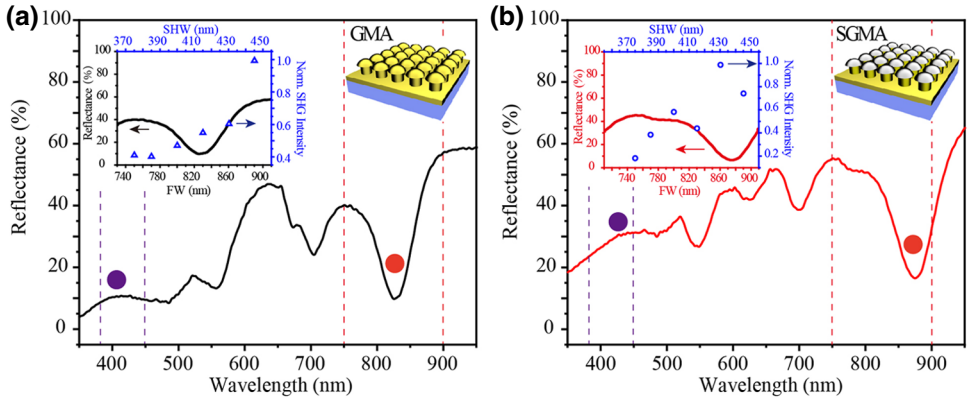

FIG. 4. Measured reflectance spectra of (a) GMA (black curve) and (b) SGMA (red curve). Insets in (a) and (b) show the corresponding wavelength-dependent SHG intensity distributions in GMA (blue triangle dots) and SGMA (blue circle dots), as well as corresponding enlarged reflectance spectra near fundamental wavelengths and schematics of GMA and SGMA, respectively. All peak values in insets in (a) and (b) are normalized by data at 445 and 430 nm, respectively.

from interband-transition suppression to plasmon-driven enhancement, resulting in the remarkable amplification of PESHG at all frequencies participating in signal emissions, as shown in the case of SMA [Fig. 3(b)].

IV. DOUBLY RESONANT DESIGNS

In light of PESHG mechanisms, the PESHG field is connected with surface susceptibilities ($\overleftrightarrow{\chi}_{surf}$) and local-field enhancements at both excitation and emission frequencies. Regarding $\overleftrightarrow{\chi}_{surf}$, because of centrosymmetry-breaking limits ($\overleftrightarrow{\chi}_{bulk} = \overleftrightarrow{0}$) for isotropic materials (gold and silver), different elements of the $\overleftrightarrow{\chi}_{surf}$ tensor with a given Ag:Au ratio can be regarded as a single nonvanishing element, $\overleftrightarrow{\chi}_{nnn}$, which denotes the normal component of surface susceptibilities [13,24]. For various Ag:Au ratios, these nonvanishing elements resemble one another [25]. Then, the local-field enhancement of PESHG should be given approximately by

$$M(\omega, 2\omega) = |L(2\omega)|^2 |L(\omega)|^4, \tag{1}$$

where $L(\Omega)$, $\Omega = \omega$ or 2ω, denotes the local-field enhancement through $L(\Omega) = E_{loc}(\Omega)/E_0(\Omega)$; $E_{loc}(\Omega)$ and $E_0(\Omega)$ denote local-field amplitudes and electric far-field amplitudes, respectively, at excitation and reemission frequencies [24]. Based on Eq. (1), we can theoretically estimate the possible maximum value of electromagnetic-field enhancement factors in "hot spots" at both excitation and reemission steps. Associated enhancement factors that contribute to PESHG processes at different steps can therefore be described as $M(\omega) = |L(\omega)|^4$ and $M(2\omega) = |L(2\omega)|^2$, respectively [26]. Furthermore, upon considering the symmetry (orientation) of local modes and nonlinear polarizations within the "hot spot" area, the relationship between measured PESHG intensities and local-field enhancements can be approximately given as

$$I_{SHG} \propto M(\omega, 2\omega) = |L(2\omega)|^2 |L(\omega)|^4, \tag{2}$$

demonstrating that efficient PESHG intensities are tightly linked to associated local-field distributions. The two-step simulation resembles the processing method for evaluating the surface-enhanced Raman scattering (SERS) enhancement factor [27]. It should be pointed out that, for more accurately evaluating the SH field in plasmon-enhanced nonlinear scattering processes, the surface integral that takes into account nonlinear polarizations in different parts and boundary conditions at the nanoscale configuration surface should be further considered [13,28]. Due to the discrepancy between the surface-integrated signal estimation and the maximum local-field enhancement correction, the experimentally obtained signal amplification is generally much smaller than that of calculated local-field enhancements.

The ability of mushroomlike geometries to confine the electromagnetic energy into subwavelength volumes is verified by means of refractive-index sensing, SERS, and extraordinary optical transmission [29–31]. To further understand characteristics of plasmonic resonances for our proposed mushroomlike geometries, we measure g-dependent reflectance spectra of SMA [Fig. 5(a)]. The SMA with $g = 10$ nm exhibits several reflectance dips (D1 to D6), ranging from NUV to near-infrared spectral regions. Particularly, dips D1 and D2 near 860 and 430 nm, respectively, overlap with excitation and emission frequencies (red and purple solid circles, respectively), which suggests that plasmonic fields excited at both fundamental and SH wavelengths exhibit a doubly resonant design in PESHG processes. In the case of SMA with $g = 0$ nm and $g < 0$ nm, with decreasing g, dips D1, D3, and D4 gradually disappear; dip D5 conspicuously increases; and dips D6 and D2 remain almost the same. Numerical analyses provide more insights into various plasmonic resonances. To obtain the results in Figs. 5(b)–5(d), we carry out 3D finite-difference time-domain simulations to demonstrate the far-field reflectance spectrum of SMA, as well as local-field distributions and electromagnetic-field vectors at various plasmonic resonances. See the Supplemental Material [16] for detailed simulated methods. Optical constants of gold and silver are taken from Ref. [32]. Simulated results displayed in Fig. 5(b) show excellent agreement with the experimental counterpart in Fig. 5(a). The difference in the strength of reflectance dips between results obtained by using these two methods can be explained by the fact that the shape of individual mushrooms in experiments varies inevitably. The local-field distribution at D5 is modulated by collective surface modes propagating on the convex surface of mushrooms in the array along the x axis, while electromagnetic fields at D4, D3, and D1 are primarily concentrated near the end point of mushroom umbrellas and gradually redistributed in the intracavity region between two adjacent mushrooms [Fig. 5(c)]. Appendix A provides more calculated results, which can be utilized for identifying the physical origin of dips D6, D5, and D2. Based on this analysis, we can reasonably deduce that umbrella-related dips D4, D3, and D1 originate from the plasmon hybridization of both interpileuse-gap resonances and pileuse-substrate cavity modes between adjacent mushrooms in 3D space, while dip D6 is attributed to the $(-1, 0)$ surface plasmon polariton (SPP) mode at the silver-air interface, and D5 originates from plasmon hybridization between collective surface modes and pileuse-substrate cavity modes; D2 originates from plasmon hybridization between collective surface modes and interpileuse-gap resonances. Furthermore, the near-field distributions of plasmonic fields excited at both 860 and 430 nm spatially overlap with each other within regions of gap-cavity spaces [Fig. 5(d)]. Fortunately, the near-field distribution is primarily concentrated near the end

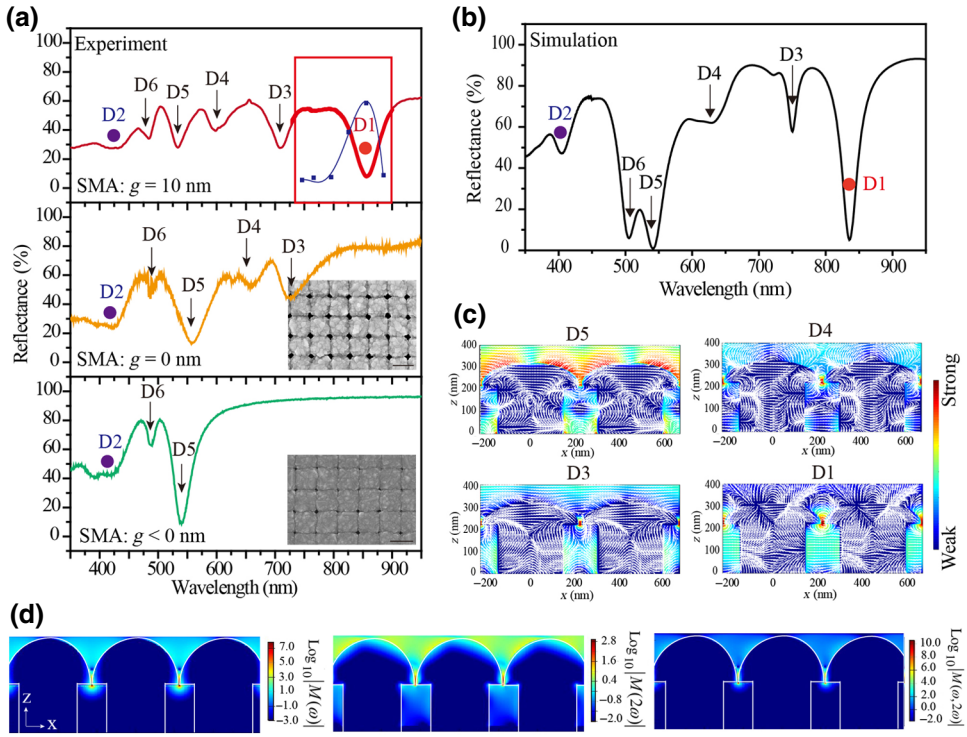

FIG. 5. (a) Measured g-dependent reflectance spectra of SMA, with $g = 10$ nm (red curve), $g = 0$ nm (orange curve), and $g < 0$ nm (green curve), while keeping other geometrical parameters constant. The red box shows the corresponding wavelength-dependent SHG intensity distribution of SMA with $g = 10$ nm (blue squares). The blue fitting line denotes a polynomial fitting function. All peak values are normalized by data at 860 nm. Insets show corresponding top-view SEM images of SMA with $g = 0$ nm and $g < 0$ nm. Scale bars, 500 nm. (b) Simulated reflectance spectrum of SMA with $g = 10$ nm. (c) Simulated local-field distributions (logarithmic scale) and electromagnetic-field vectors mapped on the x-z plane for D5, D4, D3, and D1, respectively. (d) Simulated local-field enhancements in PESHG processes (logarithmic scale), (left) excitation modes (860 nm), (middle) emission modes (430 nm), and (right) local-field enhancements that contribute to PESHG processes at different steps.

point of mushroom umbrellas, and the electric moment is aligned with the orientation of $\overleftrightarrow{\chi}_{\mathrm{nnn}}$ in the interpileuse-gap region. A well-defined symmetry (orientation) matching between local modes at different frequencies and $\overleftrightarrow{\chi}_{\mathrm{surf}}$ within the hot spot region results in the generation of strong nonlinear currents in the gap-cavity region, contributing to the boosting of conversion efficiencies. See the Supplemental Material [16] for a schematic illustration of symmetry matching between local modes and surface susceptibilities in SMA. The role of gap-cavity resonances played in the generation of nonlinear polarizations has further appeared via conducting pump-polarization-dependent SHG performances in Appendix B. The spectral position of the maximum PESHG intensity in SMA agrees satisfactorily with that of dip D1 [Fig. 5(a), inset], revealing that efficient PESHG emissions at NUV frequencies can be captured through effectively utilizing doubly resonant designs, when the effect of interband-transition suppression is avoided.

V. CONCLUSIONS

We experimentally demonstrate highly efficient PESHG emissions at NUV frequencies in a model of 3D mushroom arrays fabricated by the nanoimprint lithography followed by electrochemical deposition processes. The mushroomlike geometry features reduced centrosymmetry in three dimensions, and its SHG emissions greatly outperform emissions from unpatterned metallic films. Due to the onset of interband transitions of gold at emission steps, PESHG emission powers show a drastically decreasing trend at NUV frequencies. Through introducing plasmonic materials with higher interband-transition threshold values, we can observe the energy-transfer phenomenon of interband-transition suppression to multimode matching and finally achieve a remarkable enhancement of PESHG emissions at NUV frequencies. Our work will provide insights for quantitatively understanding the physical mechanism of plasmon-enhanced nonlinear optical processes and benefit ultralow-threshold,

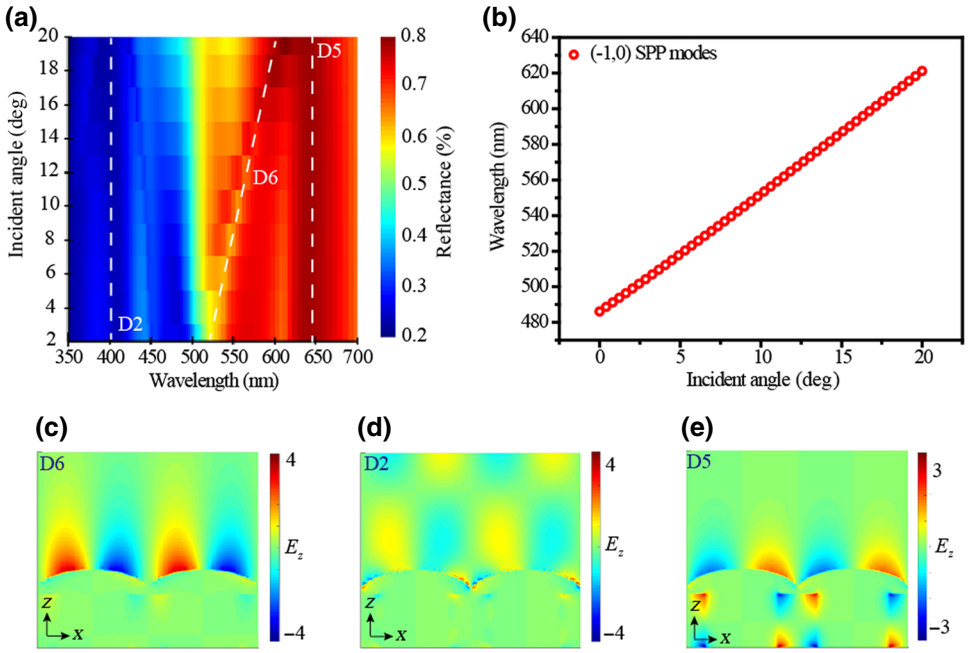

FIG. 6. (a) Simulated incident-angle-dependent reflectance spectra of SMA. White dashed lines indicate the change of spectral positions of dips D2, D6, and D5. (b) Calculated wavelengths of the $(-1, 0)$ SPP mode as a function of incident angles. Simulated near-field distributions (E_z) mapped on the x-z plane for (c) D6, (d) D2, and (e) D5, respectively.

efficient, and reproducible nonlinear wavelength conversion for quantum-optical and nonlinear metamaterial applications.

ACKNOWLEDGMENTS

We would like to thank Professor Jimin Zhao, Professor Deyin Wu, Professor Dangyuan Lei, Professor Jinfeng Zhu, Professor Zhiyuan Li, and Dr. Weimin Yang for experimental assistance and helpful discussions. This work is supported by the National Natural Science Foundation of China (Grants No. 91850119 and No. 21673192), MOST (Grants No. 2016YFA0200601 and No. 2017YFA0204902), and the Scientific Research Funds of Huaqiao University.

S. Shen and J. Shan contributed equally to this work.

APPENDIX A: IDENTIFICATION OF THE PHYSICAL ORIGIN OF DIPS D6, D5, AND D2

To provide more insights into dips D6, D5, and D2, simulated incident-angle-dependent reflectance spectra of SMA are given in Fig. 6(a). These results demonstrate that, as incident angles increase from 2° to 20°, dip D6 experiences a redshift, and dips D2 and D5 remain unchanged. For a square lattice, based on the momentum-matching condition between propagating surface plasmon modes and in-plane wavevectors of incident lights, the calculated wavelength of $(-1, 0)$ SPP modes [Fig. 6(b)] is in good agreement with that of D6 [Fig. 6(a)], confirming that D6 originates from the $(-1, 0)$ SPP mode at the silver-air interface [Fig. 6(c)]. The simulated near-field distribution at D2 exhibits a local-field enhancement trapped between the nearly touching semicylinders [Fig. 6(d)]. Thus, the origin of dip D2 can be attributed to the plasmon hybridization between collective surface modes propagating on the convex surface and localized surface plasmon resonances originated from lightning-rod effects. The simulated near-field distribution at D5 also reveals plasmon hybridization between collective surface modes and pileuse-substrate cavity resonances between adjacent mushroom units [Fig. 6(e)].

APPENDIX B: POLARIZATION-DEPENDENT SHG MEASUREMENTS

We measure pump-polarization-dependent SHG in SMA with $g = 10$ nm. As shown in Fig. 7, the maximum emission intensity periodically emerges at p-polarization

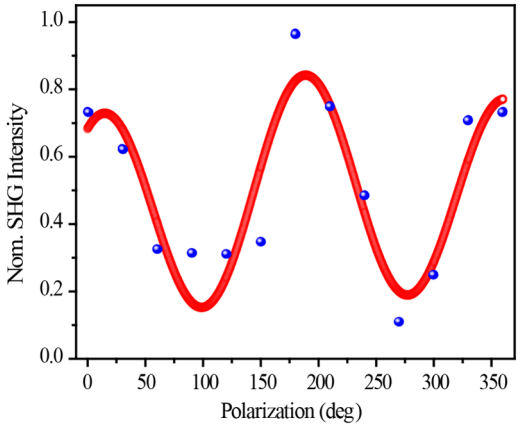

FIG. 7. Normalized SHG peak values (blue dots) as a function of incident polarization angles. Red circles denote the polynomial fitting function.

angles corresponding to $m\pi$ ($m = 0, 1, 2$). For a square lattice, interpileuse-gap resonances can be excited by either the p- or s-polarization incident beam, while the pileuse-substrate cavity mode can be excited only using the oblique p-polarization incident beam. For this reason, plasmon hybridization between two types of resonances can be effectively excited by oblique p-polarization incident beams, and the interpileuse-gap resonance under s-polarization light excitation can be considered to resemble that under the normal incident-light excitation. Thus, the maximum value of p-polarization-dependent SHG performances confirms that plasmon hybridization featuring gap-cavity resonances plays a significant role in nonlinear signal enhancements, and the introduction of pileuse-substrate cavity modes excited by oblique incident beams compensates for plasmon-enhanced nonlinear scattering processes.

[1] K. Q. Lin, S. Bange, and J. M. Lupton, Quantum interference in second-harmonic generation from monolayer WSe_2, Nat. Phys. **15**, 242 (2019).

[2] G. X. Li, S. Zhang, and T. Zentgraf, Nonlinear photonic metasurfaces, Nat. Rev. Mater. **2**, 17010 (2017).

[3] X. Y. Zhang, Q. T. Cao, Z. Wang, Y. X. Liu, C. W. Qiu, L. Yang, Q. H. Gong, and Y. F. Xiao, Symmetry-breaking-induced nonlinear optics at a microcavity surface, Nat. Photonics **13**, 21 (2019).

[4] Y. Li, M. Kang, J. J. Shi, K. Wu, S. P. Zhang, and H. X. Xu, Transversely divergent second harmonic generation by surface plasmon polaritons on single metallic nanowires, Nano Lett. **17**, 7803 (2017).

[5] R. Luo, Y. He, H. X. Liang, M. X. Li, J. W. Ling, and Q. Lin, Optical Parametric Generation in a Lithium Niobate Microring with Modal Phase Matching, Phys. Rev. Appl. **11**, 034026 (2019).

[6] M. Celebrano, X. Wu, M. Baselli, S. Grossmann, P. Biagioni, A. Locatelli, C. D. Angelis, G. Cerullo, R. Osellame, B. Hecht, L. Duo, F. Ciccacci, and M. Finazzi, Mode matching in multiresonant plasmonic nanoantennas for enhanced second harmonic generation, Nat. Nanotechnol. **10**, 412 (2015).

[7] S. D. Liu, E. S. P. Leong, G. C. Li, Y. D. Hou, J. Deng, J. H. Teng, H. C. Ong, and D. Y. Lei, Polarization-independent multiple Fano resonances in plasmonic nonamers for multimode-matching enhanced multiband second-harmonic generation, ACS Nano **10**, 1442 (2016).

[8] H. Aouani, M. Navarro-Cia, M. Rahmani, T. P. H. Sidiropoulos, M. Hong, R. F. Oulton, and S. A. Maier, Multiresonant broadband optical antennas as efficient tunable nanosources of second harmonic light, Nano Lett. **12**, 4997 (2012).

[9] B. Metzger, L. L. Gui, J. Fuchs, D. Floess, M. Hentschel, and H. Giessen, Strong enhancement of second harmonic emission by plasmonic resonances at the second harmonic wavelength, Nano Lett. **15**, 3917 (2015).

[10] B. Metzger, L. L. Gui, and H. Giessen, Ultrabroadband chirped pulse second-harmonic spectroscopy: Measuring the frequency-dependent second-order response of different metal films, Opt. Lett. **39**, 5293 (2014).

[11] L. Dreesen, C. Humbert, M. Celebi, J. J. Lemaire, A. A. Mani, P. A. Thiry, and A. Peremans, Influence of the metal electronic properties on the sum-frequency generation spectra of dodecanethiol self-assembled monolayers on Pt (111), Ag (111) and Au (111) single crystals, Appl. Phys. B-Lasers O. **74**, 621 (2002).

[12] B. Ai, P. P. Gu, Z. Y. Wang, H. Möhwald, L. M. Wang, and G. Zhang, Light trapping in plasmonic nanovessels, Adv. Optical Mater. **5**, 1600980 (2017).

[13] Y. Zhang, N. K. Grady, C. Ayala-Orozco, and N. J. Halas, Three-dimensional nanostructures as highly efficient generators of second harmonic light, Nano Lett. **11**, 5519 (2011).

[14] F. Wang, A. B. F. Martinson, and H. Harutyunyan, Efficient nonlinear metasurface based on nonplanar plasmonic nanocavities, ACS Photonics **4**, 1188 (2017).

[15] A. Artar, A. A. Yanik, and H. Altuga, Fabry–Pérot nanocavities in multilayered plasmonic crystals for enhanced biosensing, Appl. Phys. Lett. **95**, 051105 (2009).

[16] See the Supplemental Material at http://link.aps.org/supplemental/10.1103/PhysRevApplied.13.024045 for detailed fabrication schemes, SHG experimental methods, simulated methods, corresponding g-dependent mushroom arrays and SHG signal distributions, and a schematic illustration of symmetry-matching conditions.

[17] S. Shen, L. Y. Meng, Y. Zhang, J. Han, Z. Ma, S. Hu, Y. He, J. F. Li, B. Ren, T.-M. Shih, Z. H. Wang, Z. L. Yang, and Z. Q. Tian, Plasmon-enhanced second-harmonic generation nanorulers with ultrahigh sensitivities, Nano Lett. **15**, 6716 (2015).

[18] C. K. Chen, A. R. B. de Castro, and Y. R. Shen, Surface-enhanced Second-Harmonic Generation, Phys. Rev. Lett. **46**, 145 (1981).

[19] A. Slablab, L. Le Xuan, M. Zielinski, Y. de Wilde, V. Jacques, D. Chauvat, and J.-F. Roch, Second-harmonic generation from coupled plasmon modes in a single dimer of gold nanospheres, Opt. Express **20**, 220 (2012).

[20] B. R. Cooper, H. Ehrenreich, and H. R. Philipp, Optical properties of noble metals. II., Phys. Rev. A **138**, 494 (1965).

[21] A. Sobhani, A. Manjavacas, Y. Cao, M. J. McClain, F. J. de Abajo, P. Nordlander, and N. J. Halas, Pronounced linewidth narrowing of an aluminum nanoparticle plasmon resonance by interaction with an aluminum metallic film, Nano Lett. **15**, 6946 (2015).

[22] H. Ehrenreich and H. R. Philipp, Optical properties of Ag and Cu, Phys. Rev. **128**, 1622 (1962).

[23] L. Carletti, S. S. Kruk, A. A. Bogdanov, C. De Angelis, and Y. Kivshar, High-harmonic generation at the nanoscale boosted by bound states in the continuum, Phys. Rev. Res. **1**, 023016 (2019).

[24] G. Bachelier, I. Russier-Antoine, E. Benichou, C. Jonin, and P. F. Brevet, Multipolar second-harmonic generation in noble metal nanoparticles, J. Opt. Soc. Am. B **25**, 955 (2008).

[25] D. Krause, C. W. Teplin, and C. T. Rogers, Optical surface second harmonic measurements of isotropic thin-film metals: Gold, silver, copper, aluminum, and tantalum, J. Appl. Phys. **96**, 3626 (2004).

[26] S. I. Bozhevolnyi, J. Beermann, and V. Coello, Direct Observation of Localized Second-Harmonic Enhancement in Random Metal Nanostructures, Phys. Rev. Lett. **90**, 197403 (2003).

[27] J. Ye, F. F. Wen, H. Sobhani, J. B. Lassiter, P. Van Dorpe, P. Nordlander, and N. J. Halas, Plasmonic nanoclusters: Near field properties of the Fano resonance interrogated with SERS, Nano Lett. **12**, 1660 (2012).

[28] J. Butet, S. Dutta-Gupta, and O. J. F. Martin, Surface second-harmonic generation from coupled spherical plasmonic nanoparticles: Eigenmode analysis and symmetry properties, Phys. Rev. B **89**, 245449 (2014).

[29] Y. Shen, J. H. Zhou, T. R. Liu, Y. T. Tao, R. B. Jiang, M. X. Liu, G. H. Xiao, J. H. Zhu, Z. K. Zhou, X. H. Wang, C. J. Jin, and J. F. Wang, Plasmonic gold mushroom arrays with refractive index sensing figures of merit approaching the theoretical limit, Nat. Commun. **4**, 2381 (2013).

[30] J. D. Caldwell, O. Glembocki, F. J. Bezares, N. D. Bassim, R. W. Rendell, M. Feygelson, M. Ukaegbu, R. Kasica, L. Shirey, and C. Hosten, Plasmonic nanopillar arrays for large-area, high-enhancement surface-enhanced Raman scattering sensors, ACS Nano **5**, 4046 (2011).

[31] W. D. Li, J. Hu, and S. Y. Chou, Extraordinary light transmission through opaque thin metal film with subwavelength holes blocked by metal disks, Opt. Express **19**, 21098 (2011).

[32] P. B. Johnson and R. W. Christy, Optical constants of the noble metals, Phys. Rev. B **6**, 4370 (1972).